CHEMISTRY

Three-dimensional graphene nanoribbons as a framework for molecular assembly and local probe chemistry

Shigeki Kawai[1]*, Ondřej Krejčí[2], Tomohiko Nishiuchi[3], Keisuke Sahara[3], Takuya Kodama[3], Rémy Pawlak[4], Ernst Meyer[4], Takashi Kubo[3]*, Adam S. Foster[2,5,6]*

Recent advances in state-of-the-art probe microscopy allow us to conduct single molecular chemistry via tip-induced reactions and direct imaging of the inner structure of the products. Here, we synthesize three-dimensional graphene nanoribbons by on-surface chemical reaction and take advantage of tip-induced assembly to demonstrate their capability as a playground for local probe chemistry. We show that the radical caused by tip-induced debromination can be reversibly terminated by either a bromine atom or a fullerene molecule. The experimental results combined with theoretical calculations pave the way for sequential reactions, particularly addition reactions, by a local probe at the single-molecule level decoupled from the surface.

INTRODUCTION

A chemical reaction proceeds by the impacts of more than two molecules (atoms) or reactive moieties, resulting in the recombination of chemical bonds between reacted atoms and resulting in a different molecular structure. In general, most chemical reactions are conducted in bulk conditions to evenly react all molecules. Therefore, controlling a single molecule by hand, called local probe chemistry, has attracted great attention from synthesis chemists.

Atomic force microscopy (AFM) has become an important technique in the field of on-surface chemistry, since the tip terminated with a small carbon monoxide (CO) molecule allows us to observe the inner structures of molecules on surfaces (*1*). This direct observation has been used to study single (*2*, *3*) and self-assembled molecules (*4*–*6*), as well as the products of on-surface chemical reactions (*7*–*9*). Besides using AFM as a tool to identify inner structures, the local probe can be used to generate highly reactive radical species by tip-induced dehydrogenation, dehalogenation, or deoxidization on surfaces (*10*–*13*). However, since these organic redox reactions were conducted with planar molecules, the molecule-substrate interaction has to be reduced by inserting thin insulating films. In contrast, if a three-dimensional (3D) hydrocarbon is used, we can use the out-of-plane moiety for local probe chemistry, in a similar way to recent measurements of intermolecular interactions (*14*).

Here, we demonstrate synthesis of 3D graphene nanoribbons (3D-GNRs) by on-surface chemical reaction, on which local probe chemistry is conducted with an AFM tip at low temperature. A radical species was obtained by cleaving the out-of-plane C–Br σ bond with applied bias voltages and was subsequently mechanically terminated with a single Br atom and a C_{60} fullerene molecule.

[1]International Center for Materials Nanoarchitectonics, National Institute for Materials Science, 1-1, Namiki, Tsukuba, Ibaraki 305-0044, Japan. [2]Department of Applied Physics, Aalto University, P.O. Box 11100, FI-00076 Aalto, Finland. [3]Department of Chemistry, Graduate School of Science, Osaka University, Toyonaka 560-0043, Japan. [4]Department of Physics, University of Basel, Klingelbergstrasse 82, CH-4056 Basel, Switzerland. [5]WPI Nano Life Science Institute (WPI-NanoLSI), Kanazawa University, Kakuma-machi, Kanazawa 920-1192, Japan. [6]Graduate School Materials Science in Mainz, Staudinger Weg 9, 55128 Mainz, Germany.
*Corresponding author. Email: kawai.shigeki@nims.go.jp (S.K.); kubo@chem.sci.osaka-u.ac.jp (T.K.); adam.foster@aalto.fi (A.S.F.)

RESULTS

Figure 1A shows the used chemical reaction with halo-substituted molecules (*15*, *16*). By depositing precursor molecules on metal surfaces and subsequent annealing, 2D-GNRs with given widths and edge structures have been synthesized (*17*). Following this idea, we designed a precursor molecule; hexabromo-substituted trinaphtho[3.3.3]propellane (6Br-TNP) (*18*), in which two hydrogen atoms at the edge of each naphthalene moiety are substituted with bromine atoms (Fig. 1B). We deposited 6Br-TNP molecules on Au(111) and annealed at 180°C. Figure 1C shows the scanning tunneling microscopy (STM) topography, in which 1D structures can be seen. The dissociated bromine atoms on the surface (inset of Fig. 1C and fig. S1) indicate that the chemical reaction took place (Fig. 1A). The Br atoms were desorbed from the surface by annealing at higher temperature (400°C), while the 1D structure remains (Fig. 1D). After annealing at 470°C, planar structures appeared in part of the 1D structure (fig. S2). To investigate each structure, we obtained the close-up STM topographies (Fig. 1E). For each line, two bright spots are observed perpendicular to the longitudinal axis of the 1D structure, which correspond to the outmost bromine atoms. Therefore, as designed, the molecules were connected to each other, while each unit adsorbs in an upright configuration (*14*). We also obtained close-up STM topography of the structure after annealing at 400°C for 30 min (Fig. 1F). Since some of the Br atoms are missing as indicated by arrows, the out-of-plane C–Br bond can also be cleaved thermally without Au surface catalysis. The calculated bond energy is 3.8 eV, according to our calculations, which is apparently not high enough to prevent bond breaking during high-temperature annealing. Nevertheless, both the structures are, at a glance, identical, as two Br atoms in each unit point vertically out. However, we found that the gap between units actually becomes shorter after high-temperature annealing [Fig. 1, E (1.05 nm) and F (0.90 nm)]. Our density functional theory (DFT) calculations and corresponding simulated STM images show the structures: an organometallic compound (OMC) (fig. S3) and a 3D-GNR (fig. S4). The Br atoms of 3D-GNR are by ~0.05 nm lower than those of the OMC, which also has a higher conductivity due to its direct chemical bonding to the Au surface. This can also be correlated to the apparent height difference in the STM topographies.

Figure 1 (G to I) shows the summary of the chemical reaction. The deposited molecule has an upright configuration on Au(111) (Fig. 1G).

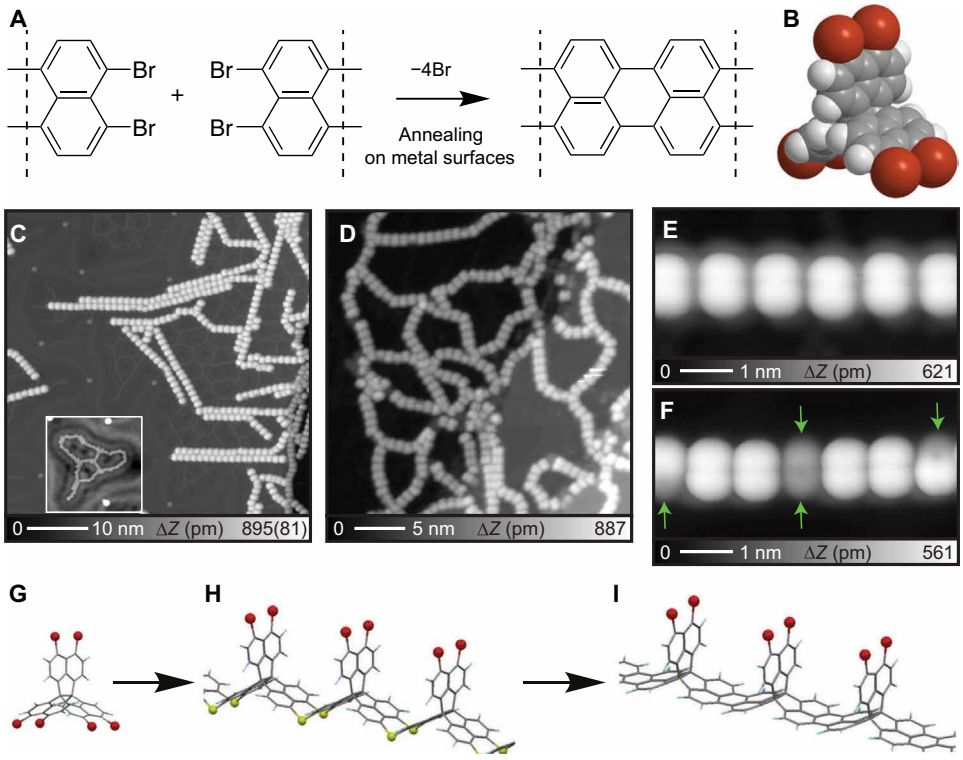

Fig. 1. Synthesis of 3D-GNR. (**A**) Ullmann-type on-surface chemical reaction. (**B**) Chemical structure of 6Br-TNP. Scanning tunneling microscopy (STM) topographies after annealing at (**C**) 180° and (**D**) 400°C. Inset in (C) shows the dissociated bromines on Au(111). (**E** and **F**) Corresponding close-up STM topographies. Green arrows indicate the thermally disrobed bromine sites. Sketch of the on-surface chemical reaction with 6Br-TNP: (**G**) schematic drawings of 6Br-TNP, (**H**) 3D-OMC, and (**I**) 3D-GNR. Measurement parameters: sample bias voltage, $V = 200$ mV. Tunneling current: $I = 0.8$ pA in (C) and (D), $I = 1$ pA in (E), and $I = 0.8$ pA in (F).

Through a gold catalytic reaction activated at 180°C, the four C–Br σ bonds in the surface vicinity are cleaved off, subsequently forming an organometallic assembly (Fig. 1H). Our DFT calculations revealed that Au adatoms are part of the OMC. The calculated reaction coordinate for this reaction, together with discussion, can be found in the Supplementary Materials. The OMC is rigid enough to prevent tip-induced lateral manipulation (fig. S5). Annealing at 400°C leads to the conjugation of the units with each other, and 3D-GNR is formed (Fig. 1I). Since the C–Br bonding energy is 3.8 eV, most of the Br atoms remain in the 3D-GNR structure during brief annealing.

The out-of-plane C–Br bond in either the OMC or 3D-GNR is an ideal playground for tip-induced chemical reaction due to the in-line configuration. We first attempted the debromination by exciting the C–Br bond with an applied voltage. In contrast to previous work with a planar molecule (*13*), the C–Br is isolated from the substrate, so the charge transfer effects are negligible. Therefore, it is expected that the bond-cleaving mechanism is similar to that shown on insulating substrates like NaCl (*19*, *20*). First, the Au tip was positioned at the target Br atom site on the OMC as indicated by an arrow (Fig. 2A). Then, the bias voltage was swept up to 2.8 V, where an abrupt change of the tunneling current was detected (Fig. 2B). We found that the Br atom disappeared from the molecules, and a faint contrast, related to the radical, appeared in the STM topography. In this debromination process, the Br atom often attaches to the tip apex as the contrast of the STM topography became sharp enough to resolve the individual Br atoms (*21*, *22*). With the Br-functionalized tip, the C–Br bond can also be cleaved as shown in Fig. 2C. In this case, the debromination is caused at 2.5 eV, which is slightly lower than that with the Au tip (Fig. 2D). Note that the minor jump at 0.8 V is most probably related to a rearrangement of the Br atom position at the tip apex. This process is highly reproducible and controllable (Fig. 2E and fig. S6). Alternatively, if the tip was scanned over the molecule at 3 V, the C–Br bonds in the scanned area can be easily cleaved (fig. S7). In contrast to STM topography, the corresponding AFM image gives a distinct contrast (dark) at the radical, mainly relating to the height difference between the unpaired electron (radical) and Br sites (Fig. 2F and fig. S8). This tip-induced debromination can also be conducted on the 3D-GNR (fig. S9).

Next, we conduct the reversed reaction, i.e., a tip-induced bromination. Before the measurement, a single Au atom, as indicated by a blue arrow, was deposited on Au(111), as a marker, from the tip by gentle contact (Fig. 2G). Subsequently, two bromine atoms were removed step by step (Fig. 2H). Here, we attempted to conduct an additional reaction as the long-lived radical is stabilized by the manipulated Br. Figure 2J shows the corresponding Z distance dependence of the frequency shift, in which an abrupt change of the frequency shift was detected and consequently the retraction curve has a different trajectory. The STM topography shows that the radical was terminated by the Br atom again, suggesting successive tip-induced bromination (Fig. 2I). Since the tip loses the Br atom, the STM topography became blurred. Calculating the force from the frequency shift curve (*23*), we found that the attractive interaction force becomes larger (Fig. 2K). The increase of the force relates to the high reactivity of the Au tip. Nevertheless, the Au···Br–C interaction is not strong enough to cleave the Br–C σ bond by force alone.

The calculated energy potential shows that the bromination process gains an energy of 100 meV at the measured Z separation (Fig. 2L).

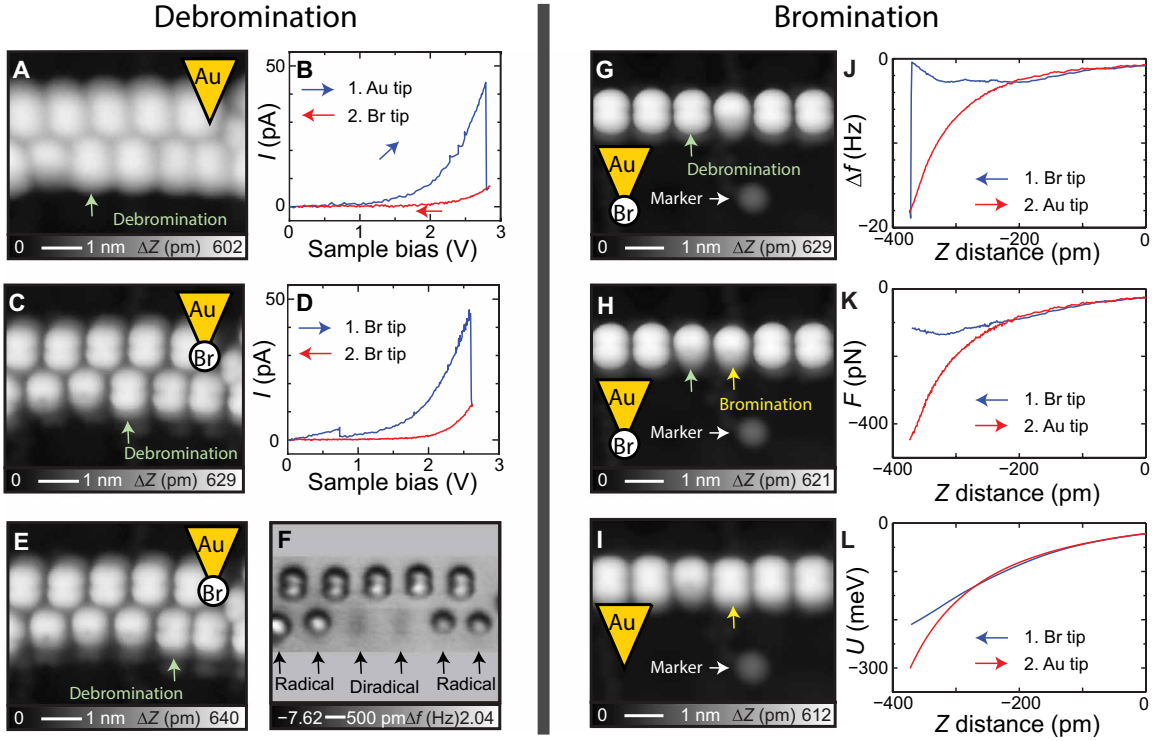

Fig. 2. Local probe chemical reaction. (**A** to **E**) A series of STM topographies during the stepwise debromination and the corresponding *I*-*V* curves during the debromination. (**F**) AFM image taken after further debromination in (E). (**G** to **I**) A series of tip-induced debromination and bromination. (**J**) Corresponding frequency shift, (**K**) force, and (**L**) energy curves during the tip-induced bromination. Measurement parameters: $V = 200$ mV and $I = 1$ pA in (A) to (I), and $V = -2$ mV and oscillation amplitude $A = 60$ pm in (J).

Note that this value does not correspond to the enthalpy change in the chemical reaction, which would be equal to the difference of the two energy minima.

Besides the tip-induced bromination, the addition reaction can be also conducted with a foreign molecule, which is the general basis of reactions in chemistry. To demonstrate this at the single-molecule level, we used a C_{60} molecule (Fig. 3A). Considering the large size of C_{60} (~1 nm), we first remove two bromines in the naphthalene moiety resulting in a 1,8-naphthyne derivative (Fig. 3B). Then, a C_{60} was picked up from the surface with a Au tip and was set close to the radical with a low bias voltage (Fig. 3C)—a large protrusion can be clearly seen at the radical part. These processes were conducted while recording the tunneling current (fig. S10). Quantum chemical calculations for four possible bonding configurations of C_{60}–1,8-naphthyne complexes revealed that the chemical bonding energies are in the −3.0 to −5.6 eV range, which is approximately half of the usual carbon-carbon single-bond energy (ca. −7.8 eV) (fig. S11). This matches with the observation that the C_{60} molecule can easily be manipulated by scanning at a lower voltage (fig. S12).

To gain deeper insight, we performed a series of DFT calculations to study the debromination process (Fig. 4A). The tip is positioned so that one (bright blue ball) of the two remaining Br atoms is just above the lowest gold atom of the tip, with the Br-Au vertical distance varying from 3.5 to 10.5 Å. For the two shortest Br-Au distances (3.5 and 4.5 Å), we performed nudged elastic band (NEB) calculations (*24*, *25*) for a Br atom moving from the molecule to the tip (Fig. 4B). The results reveal that the barriers for debromination (of the OMC) vary with the tip distance, and the calculated heights of the barrier are considerably lower than the applied voltage used for the experimental

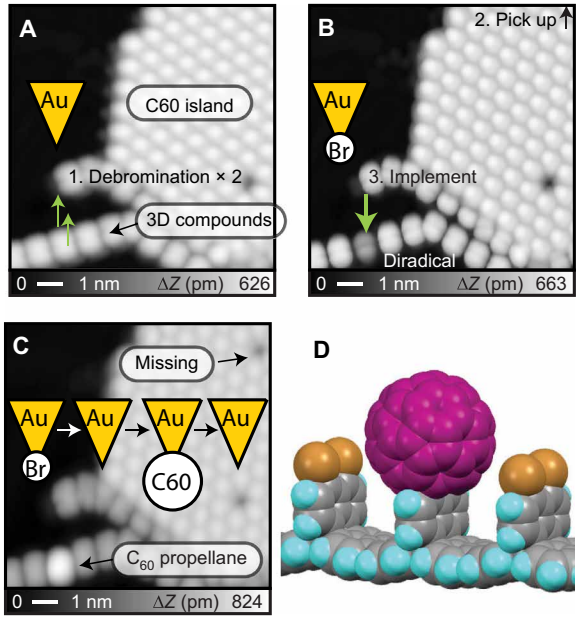

Fig. 3. Synthesis of C_{60}-propellane complex. (**A**) STM topography of a C_{60} island and 3D-OMC, taken with a Au tip. Green arrows indicate sites of the debromination. (**B**) STM topography after twice of the debromination, taken with a Br tip. A black arrow indicates the C_{60} to be picked up from the island. A green arrow indicates the site to implement the C_{60} from the tip. (**C**) STM topography after the synthesis of C_{60}-propellane complex, taken with a Au tip. Insets show the schematic drawings of the tip apex. (**D**) Schematic drawing of C_{60}-propellane complex. Measurement parameters: $V = 200$ mV and $I = 2$ pA in (A) and (B), and $V = 1500$ mV and $I = 2$ pA in (C).

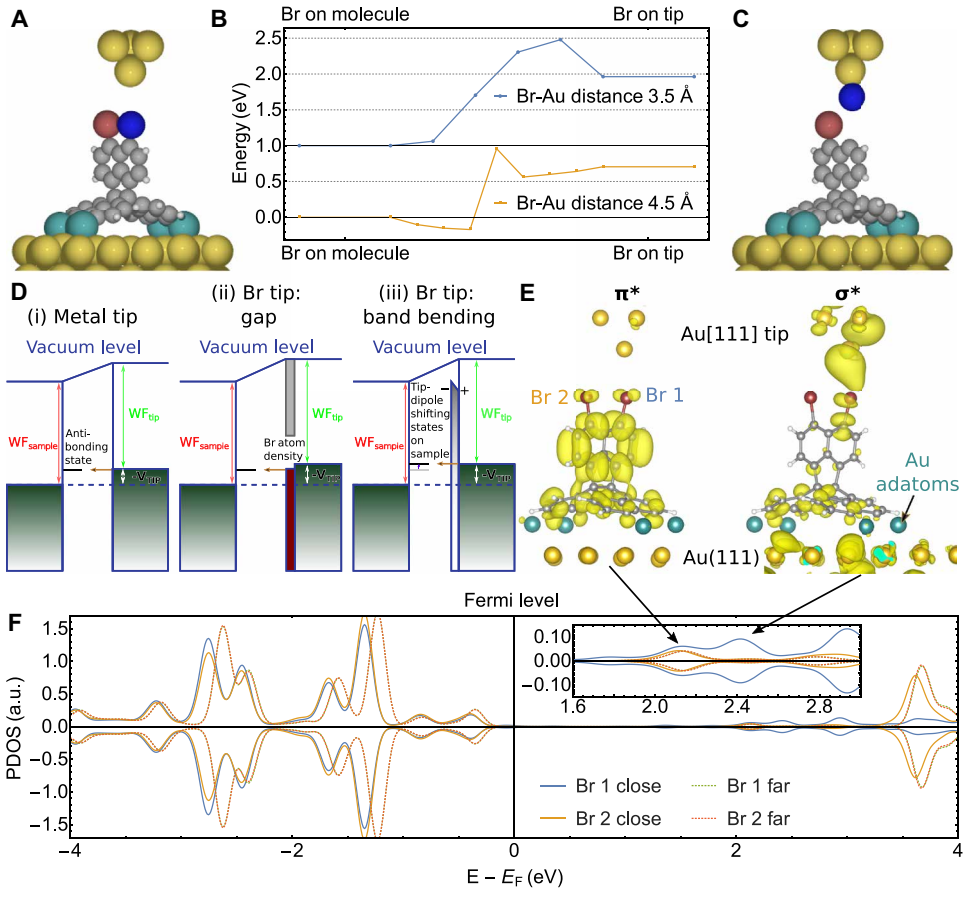

Fig. 4. Theoretical explanation of debromination and (re)bromination. (**A**) Geometry of a single unit of the OMC on the Au(111) surface with four gold adatoms (depicted in turquoise) and Au[111] tip set 4.5 Å above the reacting Br atom (blue). (**B**) Energy paths for NEB calculations for sample debromination (left to right) or bromination (right to left) for two tip heights, 3.5 and 4.5 Å. The calculated mechanical barrier for the debromination is 1 to 1.5 eV. The bromination needs only about 0.4 eV for the reaction to proceed. (**C**) Product of debromination with reacted Br atom (blue) attached to the tip. (**D**) Schematics showing presumed mechanism for the debromination—injection of electrons into antibonding state(s)—for (i) metal tip, (ii) a Br tip with gap around the Fermi level, and (iii) Br tip whose electrostatics are shifting the antibonding state to the higher energies. Both mechanisms (ii) and (iii) leads to larger bias for reaching the antibonding state(s). (**E**) 3D representation of electron density for unpopulated π* and σ* states with Au tip set 3.5 Å above the bromine atom. (**F**) Atom projected density of states (PDOS) for both Br atoms of the OMC for two cases when the tip is close (3.5 Å above the Br 1 atom) or far (10.5 Å). The inset shows, in detail, the density of the unpopulated antibonding states. The PDOS shows that the π* state has the same energy for both Br atoms without any tip distance dependency, while the σ* state is at a slightly higher energy and appears only for a very low Br-Au distance. a.u., arbitrary units.

debromination. Thus, the debromination mechanism cannot be explained in terms of a simple pumping of the energy from tunneling electrons to the C–Br bond mechanically overcoming the bond dissociation barrier. On the contrary, the barrier for the back reaction (bromination) for both paths, around 0.4 to 0.5 eV, is low enough to be overcome at experimental conditions.

The experimental evidence of different currents, but very stable sample bias for the debromination reaction with given tip type, points toward a mechanism of electron injection into an antibonding state(s), similar to earlier studies for tip-induced debrominations on insulating substrates (*19*, *20*). The population of the antibonding state(s) weakens the bond, and Br can detach by means of current heating due to inelastic electron tunneling, combined with electric field polarization and attraction to the tip. The two measured thresholds for debromination depending on the tip termination can be explained by possible mechanisms sketched in Fig. 4D. Figure 4D (i) illustrates simple injection of electrons into antibonding state(s) with the metal tip. Figure 4D (ii) shows that a gap at the tip apexes dampens the tunneling around the Fermi level of tip, while Fig. 4D (iii) depicts band bending due to electrostatics of the negative Br-terminated tip, which shifts the antibonding state(s) higher in energy. These two mechanisms result into the need to use larger voltage to populate the antibonding state(s). The electron injection mechanism is supported by our DFT calculations, which show an empty π* state at an energy of ~2.1 eV above the Fermi level. The appearance and the energy of this state do not depend on the tip height. Another antibonding state—σ* state—can be found at ~2.4 eV, if the Au tip is close to the Br atom of OMC (shown in Fig. 4, E and F). Our further calculations with Br atom added to the tip apex promotes voltage shifting mechanisms (ii) and (iii): They indicate a substantial dip of the states on the last Br and Au atom of the tip from approximately −0.2 to +0.1 eV. They also show, that the σ* state is shifted up by approximately 0.4 eV in the presence of Br on the tip. Since we do not know the real tip–Br atom distance in the experiment, we cannot establish the exact contribution of the

two antibonding states to the debromination, but it is clear that they offer a plausible mechanism for the process. Note that the applied voltage to populate the antibonding states can be slightly higher than the calculated energy, because of final conductance of the OMC and known underestimation of the gap in DFT calculations.

DISCUSSION

We demonstrate controlled addition reaction in a single molecule adsorbed on a surface by a local probe at low temperature. To demonstrate this, we synthesized a 3D-GNR, in which brominated naphthalene forms a periodic out-of-plane substructure. This bromonaphthalene is effectively isolated from the substrate and can be used as an ideal playground for local probe chemistry. The long-lived radical can be obtained by the tunneling current and stabilized by either a bromine atom or C_{60} molecule. We believe that such direct addition reactions are vital to advance our chemistry toward synthesis of single compound atom by atom.

MATERIALS AND METHODS

Experimental

All measurements were performed with a commercially available Omicron low-temperature STM/AFM system and a homemade STM/AFM system, operating in ultrahigh vacuum at below 5 K. For AFM, we used a tuning fork with a chemically etched tungsten tip as a force sensor (*26*). The resonance frequency and the mechanical quality factor are 24,756.3 and 23,484 Hz, respectively. The high stiffness of 1800 N/m realizes a stable operation with a small amplitude of 60 pm (*27*). The frequency shift, caused by the tip-sample interaction, was detected with a commercially available digital phase-locked loop (Nanonis OC4 and Zurich Instruments: HF2-LI and HF2-PLL) (*28*). For the STM measurement, the bias voltage was applied to the tip while the sample was electronically grounded in the OMICRON STM/AFM system and vice versa in our homemade STM/AFM system. To be consistent, the sample bias voltage is indicated with respect to the tip grounded. The tip apex was ex situ sharpened by milling with a focused ion beam, and the radius was less than 10 nm. Clean gold and silver tips were in situ formed by indenting to the Au and Ag sample surfaces, respectively, and applying a pulse bias voltage between tip and sample several times. Clean Au(111) and Ag(111) surfaces were in situ prepared by repeated cycles of standard Ar^+ sputtering (3×10^{-6} mbar, 1000 eV, and 15 min) and annealing at 730 and 750 K. In this experiment, 6Br-TNP molecules were deposited on the surface from crucibles of a Knudsen cell, heated at 530 K. Measured images were partially analyzed using the WSxM software (*29*).

Theoretical calculations

All DFT calculations in this work were performed with the periodic plane-wave basis Vienna Ab-Initio Simulation Package code (*30*, *31*). The spin-polarized optB86B + van der Waals (vdW)–DF functional (*32*–*34*) was used to accurately describe vdW interactions in the calculated systems. We select this functional based on previous work, where it provided comparable results with commonly used DFT-D3 (*35*) functional and Tkatchenko-Scheffler method (*36*), as well as experimental measurements (*37*, *38*). The core electrons were described using projected augmented wave method (*39*). For all calculations, we applied a kinetic energy cutoff of 550 eV; however, depending on the type of calculation, we used different precision (PREC parameters). All the energies stated in this article are: energy without entropy.

For the static calculations, presented in figs. S3 (A to C) and S13 and table S1, we used PREC = accurate. Calculations of the adsorption of 6Br-TNP molecules on the face-cubic centered Au(111) surface (fig. S11) were performed using a 6×6 Au slab with at least ~9.4 Å of vacuum above the molecule (z cell height, 30 Å). Three to five Au layers were used for a systematic check of the minimal amount of Au layers properly describing the molecular adsorption on the Au surface. Already three Au layers, with two bottom layers fixed in the geometry optimization, gives a good enough description of the Au-molecule interaction. We also systematically checked k-point convergence, with sampling chosen according to system size. We found that $7 \times 7 \times 1$ k points were enough for the calculations. The results shown in fig. S13 and table S1 concerning molecular adsorption were calculated with an even more precise $9 \times 9 \times 1$ mesh. The OMC debromination energy without STM tip was computed within the same framework as the 6Br-TNP adsorption. The calculations of projected density of states (PDOS) for a single OMC and Br tip (Fig. 4, E and F) were performed also in a 6×6 Au(111) supercell with Γ point only. The results of the calculations were checked with a $7 \times 7 \times 1$ k-point mesh as well, showing the same PDOS spectra. Calculations with two 6Br-TNP molecules, or molecular parts, were done with perpendicular $12 \times 6 \times 3$ Au slabs to reduce interaction with neighboring cells. For these calculations, we used a $3 \times 7 \times 1$ k-point mesh.

Reaction pathways shown in Fig. 4 (A to C) and fig. S14 were calculated using the NEB method (*24*). For most of these calculations, we tried to estimate the energy barrier by means of climbing NEB approach (*25*), unless stated otherwise. Because of the computational complexity of these calculations, we used only Γ point for them and PREC = normal.

SUPPLEMENTARY MATERIALS

Supplementary material for this article is available at http://advances.sciencemag.org/cgi/content/full/6/9/eaay8913/DC1

REFERENCES AND NOTES

1. L. Gross, F. Mohn, N. Moll, P. Liljeroth, G. Meyer, The chemical structure of a molecule resolved by atomic force microscopy. *Science* **325**, 1110–1114 (2009).
2. L. Gross, F. Mohn, N. Moll, G. Meyer, R. Ebel, W. M. Abdel-Mageed, M. Jaspars, Organic structure determination using atomic-resolution scanning probe microscopy. *Nat. Chem.* **2**, 821–825 (2010).

3. N. Pavliček, B. Fleury, M. Neu, J. Niedenführ, C. Herranz-Lancho, M. Ruben, J. Repp, Atomic force microscopy reveals bistable configurations of dibenzo[a,h]thianthrene and their interconversion pathway. *Phys. Rev. Lett.* **108**, 086101 (2012).
4. J. Zhang, P. Chen, B. Yuan, W. Ji, Z. Cheng, X. Qiu, Real-space identification of intermolecular bonding with atomic force microscopy. *Science* **342**, 611–614 (2013).
5. S. Kawai, A. Sadeghi, X. Feng, P. Lifen, R. Pawlak, T. Glatzel, A. Willand, A. Orita, J. Otera, S. Goedecker, E. Meyer, Obtaining detailed structural information about supramolecular systems on surfaces by combining high-resolution force microscopy with ab initio calculations. *ACS Nano* **7**, 9098–9105 (2013).
6. S. K. Hämäläinen, N. van der Heijden, J. van der Lit, S. den Hartog, P. Liljeroth, I. Swart, Intermolecular contrast in atomic force microscopy images without intermolecular bonds. *Phys. Rev. Lett.* **113**, 186102 (2014).
7. D. G. de Oteyza, P. Gorman, Y.-C. Chen, S. Wickenburg, A. Riss, D. J. Mowbray, G. Etkin, Z. Pedramrazi, H.-Z. Tsai, A. Rubio, M. F. Crommie, F. R. Fischer, Direct imaging of covalent bond structure in single-molecule chemical reactions. *Science* **340**, 1434–1437 (2013).
8. S. Kawai, V. Haapasilta, B. D. Lindner, K. Tahara, P. Spijker, J. A. Buitendijk, R. Pawlak, T. Meier, Y. Tobe, A. S. Foster, E. Meyer, Thermal control of sequential on-surface transformation of a hydrocarbon molecule on a copper surface. *Nat. Commun.* **7**, 12711 (2016).
9. O. Stetsovych, M. Švec, J. Vacek, J. V. Chocholoušová, A. Jančařík, J. Rybáček, K. Kosmider, I. G. Stará, P. Jelínek, I. Starý, From helical to planar chirality by on-surface chemistry. *Nat. Chem.* **9**, 213–218 (2017).
10. N. Pavliček, B. Schuler, S. Collazos, N. Moll, D. Pérez, E. Guitián, G. Meyer, D. Peña, L. Gross, On-surface generation and imaging of arynes by atomic force microscopy. *Nat. Chem.* **7**, 623–628 (2015).
11. B. Schuler, S. Fatayer, F. Mohn, N. Moll, N. Pavliček, G. Meyer, D. Peña, L. Gross, Reversible Bergman cyclization by atomic manipulation. *Nat. Chem.* **8**, 220–224 (2016).
12. J. Krüger, N. Pavliček, J. M. Alonso, D. Pérez, E. Guitián, T. Lehmann, G. Cuniberti, A. Gourdon, G. Meyer, L. Gross, F. Moresco, D. Peña, Tetracene formation by on-surface reduction. *ACS Nano* **10**, 4538–4542 (2016).
13. N. Pavliček, A. Mistry, Z. Majzik, N. Moll, G. Meyer, D. J. Fox, L. Gross, Synthesis and characterization of triangulene. *Nat. Nanotechnol.* **12**, 308–311 (2017).
14. S. Kawai, T. Nishiuchi, T. Kodama, P. Spijker, R. Pawlak, T. Meier, J. Tracey, T. Kubo, E. Meyer, A. S. Foster, Direct quantitative measurement of the C═O···H–C bond by atomic force microscopy. *Sci. Adv.* **3**, e1603258 (2017).
15. L. Grill, M. Dyer, L. Lafferentz, M. Persson, M. V. Peters, S. Hecht, Nano-architectures by covalent assembly of molecular building blocks. *Nat. Nanotechnol.* **2**, 687–691 (2007).
16. J. Cai, P. Ruffieux, R. Jaafar, M. Bieri, T. Braun, S. Blankenburg, M. Muoth, A. P. Seitsonen, M. Saleh, X. Feng, K. Müllen, R. Fasel, Atomically precise bottom-up fabrication of graphene nanoribbons. *Nature* **466**, 470–473 (2010).
17. H. Zhang, H. Lin, K. Sun, L. Chen, Y. Zagranyarski, N. Aghdassi, S. Duhm, Q. Li, D. Zhong, Y. Li, K. Mülle, H. Fuchs, L. Chi, On-surface synthesis of rylene-Type graphene nanoribbons. *J. Am. Chem. Soc.* **137**, 4022–4025 (2015).
18. T. Kubo, S. Miyazaki, T. Kodama, M. Aoba, Y. Hirao, H. Kurata, A facile synthesis of trinaphtho[3.3.3]propellane and its π-extension and the formation of a two-dimensional honeycomb molecular assembly. *Chem. Commun.* **51**, 3801–3803 (2015).
19. F. Mohn, B. Schuler, L. Gross, G. Meyer, Different tips for high-resolution atomic force microscopy and scanning tunneling microscopy of single molecules. *Appl. Phys. Lett.* **102**, 073109 (2013).
20. N. Pavliček, Z. Majzik, S. Collazos, G. Meyer, D. Pérez, E. Guitián, D. Peña, L. Gross, Generation and characterization of a meta-Aryne on Cu and NaCl surfaces. *ACS Nano* **11**, 10768–10773 (2017).
21. P. Hapala, G. Kichin, C. Wagner, F. S. Tautz, R. Temirov, P. Jelínek, Mechanism of high-resolution STM/AFM imaging with functionalized tips. *Phys. Rev. B* **90**, 085421 (2014).
22. O. Krejčí, P. Hapala, M. Ondráček, P. Jelínek, Principles and simulations of high-resolution STM imaging with a flexible tip apex. *Phys. Rev. B* **95**, 045407 (2017).
23. J. E. Sader, S. P. Jarvis, Accurate formulas for interaction force and energy in frequency modulation force spectroscopy. *Appl. Phys. Lett.* **84**, 1801–1803 (2004).
24. H. J'onsson, G. Mills, K. W. Jacobsen, *Classical And Quantum Dynamics In Condensed Phase Simulations* (World Scientific Singapore,1998), pp. 385–404.
25. G. Henkelman, B. P. Uberuaga, H. Jónsson, A climbing image nudged elastic band method for finding saddle points and minimum energy paths. *J. Chem. Phys.* **113**, 9901–9904 (2000).
26. F. J. Giessibl, High-speed force sensor for force microscopy and profilometry utilizing a quartz tuning fork. *Appl. Phys. Lett.* **73**, 3956–3958 (1998).
27. F. J. Giessibl, Advances in atomic force microscopy. *Rev. Mod. Phys.* **75**, 949–983 (2003).
28. T. R. Albrecht, P. Grütter, D. Horne, D. Rugar, Frequency modulation detection using high-*Q* cantilevers for enhanced force microscope sensitivity. *J. Appl. Phys.* **69**, 668–672 (1991).
29. I. Horcas, R. Fernández, J. M. Gómez-Rodríguez, J. Colchero, J. Gómez-Herrero, A. M. Baro, WSXM: A software for scanning probe microscopy and a tool for nanotechnology. *Rev. Sci. Instrum.* **78**, 013705 (2007).
30. G. Kresse, J. Furthmüller, Efficiency of ab-initio total energy calculations for metals and semiconductors using a plane-wave basis set. *Comput. Mater. Sci.* **6**, 15–50 (1996).
31. G. Kresse, J. Furthmüller, Efficient iterative schemes for ab initio total-energy calculations using a plane-wave basis set. *Phys. Rev. B* **54**, 11169–11186 (1996).
32. J. Klimeš, D. R. Bowler, A. Michaelides, Chemical accuracy for the Van der Waals density functional. *J. Phys. Condens. Matter* **22**, 022201 (2010).
33. J. Klimeš, D. R. Bowler, A. Michaelides, Van der Waals density functionals applied to solids. *Phys. Rev. B* **83**, 195131 (2011).
34. T. Björkman, A. Gulans, A. V. Krasheninnikov, R. M. Nieminen, Van der Waals bonding in layered compounds from advanced density-functional first-principles calculations. *Phys. Rev. Lett.* **108**, 235502 (2012).
35. S. Grimme, J. Antony, S. Ehrlich, H. Krieg, A consistent and accurate ab initio parametrization of density functional dispersion correction (DFT-D) for the 94 elements H-Pu. *J. Chem. Phys.* **132**, 154104 (2010).
36. A. Tkatchenko, M. Scheffler, Accurate molecular Van der Waals interactions from ground-state electron density and free-atom reference data. *Phys. Rev. Lett.* **102**, 073005 (2009).
37. S. Kawai, S. Nakatsuka, T. Hatakeyama, R. Pawlak, T. Meier, J. Tracey, E. Meyer, A. S. Foster, Multiple heteroatom substitution to graphene nanoribbon. *Sci. Adv.* **4**, eaar7181 (2018).
38. S. Kawai, O. Krejčí, A. S. Foster, R. Pawlak, X. Feng, P. Lifen, A. Orita, E. Meyer, Diacetylene linked anthracene oligomers synthesized by one-shot homocoupling of trimethylsilyl on Cu(111). *ACS Nano* **12**, 8791–8797 (2018).
39. P. E. Blöchl, Projector augmented-wave method. *Phys. Rev. B* **50**, 17953–17979 (1994).
40. P. Maksymovych, O. Voznyy, D. B. Dougherty, D. C. Sorescu, J. T. Yates Jr., Gold adatom as a key structural component in self-assembled monolayers of organosulfur molecules on Au(111). *Prog. Surf. Sci.* **85**, 206–240 (2010).
41. Y. Wang, N. S. Hush, J. R. Jeffrey, Simulation of the Au (111)–(22×√3) surface reconstruction. *Phys. Rev. B* **75**, 233416 (2007).
42. N. Kocić, X. Liu, S. Chen, S. Decurtins, O. Krejčí, P. Jelínek, J. Repp, S.-X. Liu, Control of reactivity and regioselectivity for on-Surface dehydrogenative aryl–aryl bond formation. *J. Am. Chem. Soc.* **138**, 5585–5593 (2016).
43. A. Berisha, C. Combellas, F. Kanoufi, J. Médard, P. Decorse, C. Mangeney, I. Kherbouche, M. Seydou, F. Maurel, J. Pinson, Alkyl-modified gold surfaces: Characterization of the Au–C bond. *Langmuir* **34**, 11264–11271 (2018).
44. L. Laurentius, S. R. Stoyanov, S. Gusarov, A. Kovalenko, R. Du, G. P. Lopinski, M. T. McDermott, Diazonium-derived aryl films on gold nanoparticles: Evidence for a carbon–gold covalent bond. *ACS Nano* **5**, 4219–4227 (2011).

Acknowledgments: O.K. and A.S.F. acknowledge use of the CSC and the Aalto Science-IT project for computational resources. O.K. would like to thank F. F. Canova, P. Hapala, and P. Kocán for fruitful discussion. **Funding:** This work was supported, in part, by Japan Society for the Promotion of Science (JSPS) KAKENHI grant nos. 19H00856 and 18K19004, by the Swiss National Science Foundation, by the Swiss Nanoscience Institute, by European Research Council (ERC) under the European Union's Horizon 2020 research and innovation program (grant agreement no. 834402), and by NIMS Joint Research Hub Program. O.K. and A.S.F. have been supported by the Academy of Finland (project 314877). A.S.F. has been supported by the World Premier International Research Center Initiative (WPI), MEXT, Japan. **Author contributions:** S.K. and K.S. carried out the experiment. T.N., T. Kodama, and T. Kubo synthesized the molecule. O.K. and A.S.F. carried out the DFT calculations. S.K., O.K., K.S., R.P., E.M., and A.S.F. analyzed the data. S.K., O.K., T.N., and A.S.F. wrote the manuscript, and all authors commented. S.K., T.N., and T. Kubo planned the project. **Competing interests:** The authors declare that they have no competing interest. **Data and materials availability:** All data needed to evaluate the conclusions in the paper are present in the paper and/or the Supplementary Materials. Additional data related to this paper may be requested from the authors.

Submitted 27 July 2019
Accepted 6 December 2019
Published 28 February 2020
10.1126/sciadv.aay8913

Citation: S. Kawai, O. Krejčí, T. Nishiuchi, K. Sahara, T. Kodama, R. Pawlak, E. Meyer, T. Kubo, A. S. Foster, Three-dimensional graphene nanoribbons as a framework for molecular assembly and local probe chemistry. *Sci. Adv.* **6**, eaay8913 (2020).

Science Advances

Three-dimensional graphene nanoribbons as a framework for molecular assembly and local probe chemistry

Shigeki Kawai, Ondrej Krejcí, Tomohiko Nishiuchi, Keisuke Sahara, Takuya Kodama, Rémy Pawlak, Ernst Meyer, Takashi Kubo and Adam S. Foster

Sci Adv **6** (9), eaay8913.
DOI: 10.1126/sciadv.aay8913